
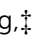






Cite this: *Chem. Sci.*, 2023, 14, 1434

All publication charges for this article have been paid for by the Royal Society of Chemistry

BOINPYs: facile synthesis and photothermal properties triggered by photoinduced nonadiabatic decay†

Lizhi Gai, ^{‡a} Ruijing Zhang, ^{‡bd} Xiuguang Shi,^a Zhigang Ni, ^a Sisi Wang,^{ac} Jun-Long Zhang, ^{*be} Hua Lu ^{*a} and Zijian Guo ^c

Photothermal agents (PTAs) represent a core component of photothermal therapy (PTT). However, the current photothermal dyes are almost derived from well-known chromophores such as porphyrins, cyanine, and BODIPYs, and the design of new chromophores as versatile building blocks for PTA is considerably challenging because of the complexity of the modulation of excited-states. Herein, we adopted the concept of photoinduced nonadiabatic decay (PIND) to develop a photothermal boron-containing indoline-3-one-pyridyl chromophore (viz. BOINPY) with a facile one-pot synthesis and high yields. BOINPY derivatives exhibited specific features that fully address the concerns related to the design of PTA. The behavior and mechanism of BOINPYs for generating heat through the conical intersection pathway, which is called PIND, have been well understood through theoretical calculations. After encapsulation into the F127 copolymer, BOINPY@F127 nanoparticles displayed efficient photothermal conversion and performed well in the treatment of solid tumors upon light irradiation with good biocompatibility. This study provides useful theoretical guidance and concrete photothermal chromophores, which offer a versatile strategy embedding tunable properties for the development of diverse high-performance PTA.

Received 22nd November 2022

Accepted 7th January 2023

DOI: 10.1039/d2sc06435a

rsc.li/chemical-science

Introduction

Cancer is one of the most deadly diseases known to humans.¹ Conventional cancer therapies including surgery, chemotherapy, and radiotherapy suffer from several limitations, such as non-specificity and various side effects.² Recently, photothermal therapy (PTT) has received significant attention for cancer

treatment owing to its low systemic toxicity, good specificity, and minimal invasiveness.³ Various photothermal agents (PTAs) based on inorganic materials and organic polymers have been prepared; although they exhibit excellent photostability and photothermal conversion, their potential for long-term toxicity and lack of biodegradability provide barriers to effective clinical efforts.⁴ Small organic molecules are ideally potential alternatives to nano-materials because they can be conceived with considerations of function, safety, and formulation, and their features can be further fine-tuned through specialized synthesis.⁵ Currently, most of the organic photothermal compounds are derived from well-known chromophores such as porphyrins,⁶ phthalocyanines,⁷ diketopyrrolopyrroles,⁸ cyanines,⁹ and BODIPY,¹⁰ whose syntheses are usually time-consuming, involving multiple steps and therefore low yields. Therefore, a rational design of molecular platforms with scale-up synthesis and high yields that exhibit high photothermal therapeutic efficacy is essential.

Photothermal effects originate from nonradiative relaxation processes.^{5a} Because photothermal agents convert the absorbed photons into heat, they generally have low fluorescence quantum yields and low yields of singlet oxygen generation. In addition, photothermal agents should ideally absorb in the red/NIR region and be highly photostable in this region.¹¹ Theoretically, the excited molecular motions can release the excitation energy as heat through the conical intersection (CI) nonradiative pathway, which is called photoinduced nonadiabatic decay (PIND). Such excited

^aCollege of Material, Chemistry and Chemical Engineering, Key Laboratory of Organosilicon Chemistry and Material Technology, Ministry of Education, Hangzhou Normal University, No. 2318, Yuhangtang Road, Hangzhou, 311121, P. R. China. E-mail: hualu@hznu.edu.cn

^bBeijing National Laboratory for Molecular Sciences, State Key Laboratory of Rare Earth Materials Chemistry and Applications, College of Chemistry and Molecular Engineering, Peking University, Beijing 100871, P. R. China. E-mail: zhangjunlong@pku.edu.cn

^cState Key Laboratory of Coordination Chemistry, Coordination Chemistry Institute, School of Chemistry and Chemical Engineering, Nanjing University, Nanjing 210023, P. R. China

^dSpin-X Institute, School of Chemistry and Chemical Engineering, South China University of Technology, Guangzhou 510641, China

^eChemistry and Chemical Engineering, Guangdong Laboratory, Shantou 515031, China

† Electronic supplementary information (ESI) available: Experimental and additional spectral data. CCDC 2142887, 2142888 and 2142890. For ESI and crystallographic data in CIF or other electronic format see DOI: <https://doi.org/10.1039/d2sc06435a>

‡ These authors contributed equally.

molecules can easily go by the nonradiative CI pathway and return to the ground state, thus PIND-guided chromophores have great potential to serve as photothermal agents.¹² Our inspiration for building the novel core skeleton of photothermal agents came from isoindoline-1-one-pyridyl difluoroboron dyes (BOISPY), reported by Xiao *et al.* as shown in Fig. 1a (left), which possess strong blue fluorescence.¹³ The low molecular orbital (MO) distribution of the phenyl ring at the isoindoline unit in the highest occupied MO (HOMO) results in an absorption wavelength in the UV region. We have previously explored the spectroscopic properties of the aza-isoindoline-1-one-pyridyl difluoroboron dye.¹⁴ Based on the previous study, herein we describe the development of a new chromophore (BOINPY) in which the isoindolinyl unit is replaced with an indolin-3-one unit through a one-step continuous reaction (Fig. 1a, right). Analysis of the results calculated indicate that this new core has a narrow bandgap relative to the reported BOISPY, which is beneficial for the red/NIR light absorbing capability (Fig. 1b, S1 and Table S1, ESI†). In addition, nucleus-independent chemical shift (NICS) calculations show that the five-membered

ring of the new chromophore exhibits weak antiaromaticity, which is conducive to the delocalization of electrons over the entire core skeleton,¹⁸ as observed in the ACID plot (Fig. 1c and d).¹⁹ Moreover, the $S_1 \rightarrow S_0$ transition corresponds to a large charge separation with a small oscillator strength ($f = 0.08$), also observed from the hole and electron distributions for the S_1 state of BOINPY (Fig. 1e and S2, ESI†); the S_1 state is spectroscopically “dark”, which inhibits the radiative processes and quenches the fluorescence. Structural CI was computed to better explain the different spectroscopic properties of the two isomers and to explore a theoretical strategy for the construction of photothermal reagents in depth.²⁰ After photoexcitation, the excited state of BOISPY relaxes to the excited state minimum (S_{1min}), and then releases the energy through radiative decay because the configurations of S_{1min} and CI are quite different and the energy gap from the S_{1min} (3.47 eV) to CI (5.22 eV) is relatively large (*ca.* 1.75 eV). In addition, there is a small barrier (0.30 eV higher than CI) along the pathway connecting S_{1min} and CI, which was approximately obtained by the linearly interpolated internal coordinates (LIICs). The radiative decay thus

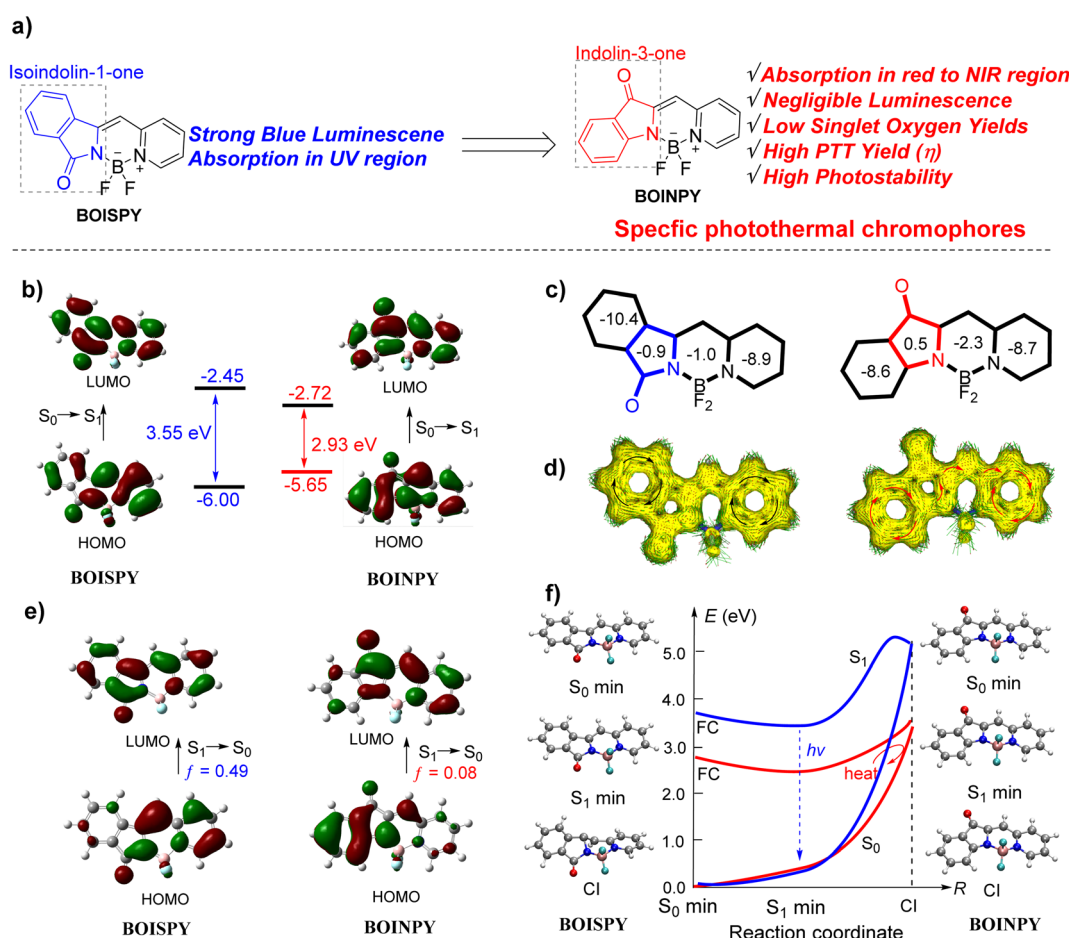


Fig. 1 (a) Structures of boron-containing isoindoline-1-one-pyridyl dyes (BOISPY) and our designed boron-containing indolin-3-one-pyridyl (BOINPY) chromophore. (b) Frontier molecular orbital (MO) energetics of the ground-state. (c) NICS(1) value. (d) ACID plot. (e) Frontier MOs of the excited S_1 state. The vertical excitation related calculations are based on the optimized ground-state geometry (S_0 state), while the emission related calculations were based on the optimized excited state (S_1 state) geometry at the B3LYP/6-31G(d,p) level.¹⁵ (f) The structures of the conical intersection (CI) were determined at the spin flip SF-BHandHLYP/6-31G(d,p) level using the GAMESS 2021 software (blue line for BOISPY and red line for BOINPY).¹⁶ All excitation energies were further calculated using the SF-BHandHLYP functional with the basis set 6-311G(d,p).¹⁷



plays a major role, and hence BOISPY exhibits strong fluorescence (Fig. 1f). However, for **BOINPY**, the gap between S_{1min} (2.56 eV) and CI (3.43 eV) is only 0.87 eV, which is energetically accessible. Further LIIC calculations show that there is no barrier. The small energy difference is somewhat because the structures of the S_{1min} and CI for **BOINPY** are almost identical (Fig. 1f and S2, ESI†). This indicates that the excited energy can easily cross through the nonradiative pathway and return to the ground state by heat. Such a chromophore core thus has significant potential to serve as the photothermal agent. This design idea based on PIND provides a significant strategy for the design of photothermal agents.

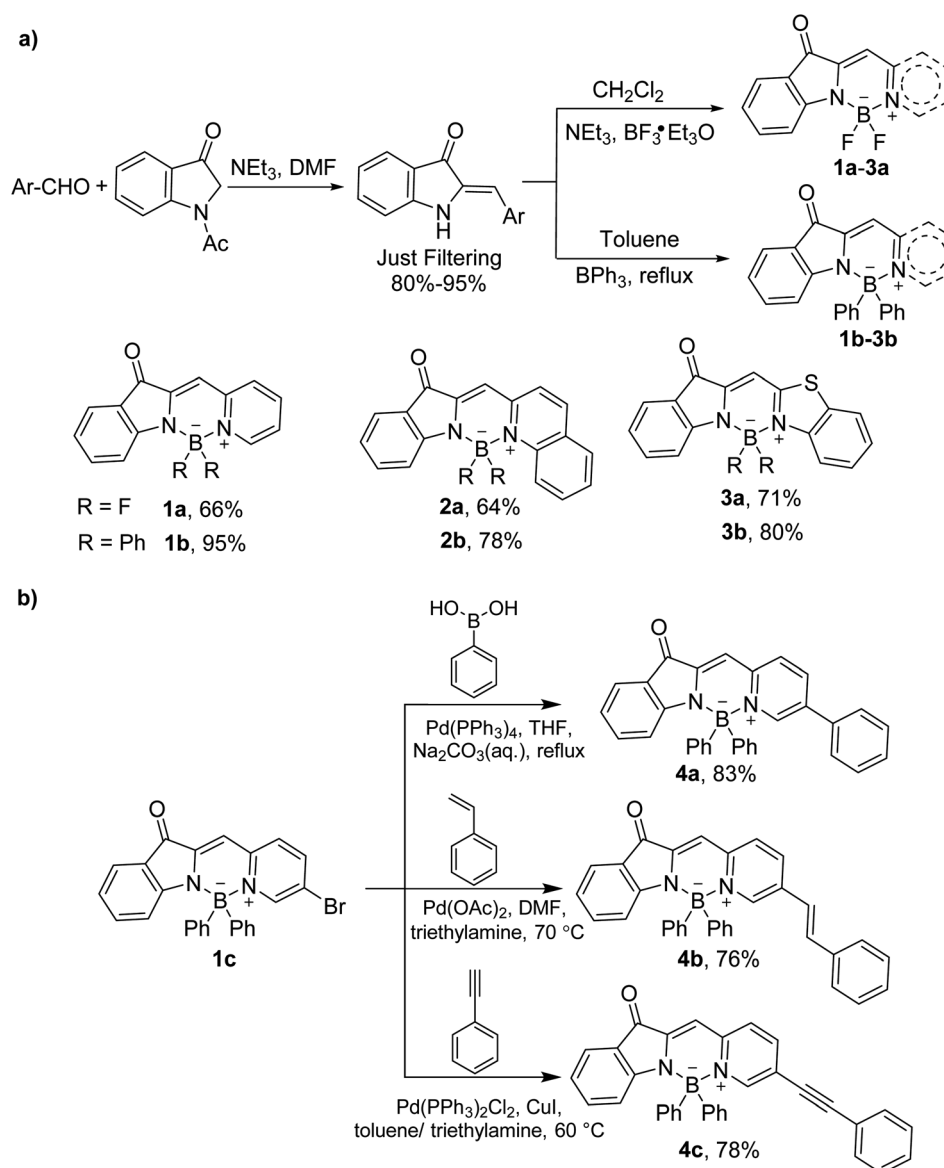
As theoretically predicted, the **BOINPY** core and its derivatives exhibited gratifying properties such as negligible emission, extremely low singlet oxygen production capability, and superior photostability; the above-mentioned features fully address the concerns related to the use of PTA in PTT. Compounds **2b** and **2b**

encapsulated in F127 copolymer (**2b@F127**) exhibited high photothermal conversion efficiencies of 57% and 44%, respectively. In addition, **2b@F127** exhibited NIR PTT capability, robust photostability and excellent biocompatibility *in vivo*.

Results and discussion

Synthesis

BOINPY was synthesized from commercially available 1-acetyl-3-indolinone *via* a one-step continuous reaction (Scheme 1a). Treatment of 1-acetyl-3-indolinone with an aromatic aldehyde in the presence of triethylamine afforded the key precursor by a simple filtration, which was trapped with $BF_3 \cdot OEt_2$ in the presence of triethylamine or with BPh_3 in refluxing toluene to obtain the target molecules **1a–3a** in yields of 64–71% and **1b–3b** in yields of 78–95%. This simple potent skeleton might prove useful to



Scheme 1 (a) Synthetic route to BOINPYs **1a–3a** and **1b–3b**. (b) Transition metal catalyzed coupling reaction of BOINPYs **4a–4c**.



enrich the structural diversity of chromophores. With the above promising synthesizing results, dye **1c**, carrying a bromide atom, was prepared according to the synthetic method of **1a**. And then it was tolerated under the conditions of Suzuki–Miyaura coupling, Heck coupling, and Sonogashira coupling and afforded phenylated (**4a**), styrylated (**4b**), and phenylethynylated (**4c**) **BOINPYs** (Scheme 1b). All these compounds were stable in air and moisture. The structures of all the **BOINPY** dyes were characterized by ^1H NMR and ^{13}C NMR spectroscopy and high-resolution MS.

X-ray single-crystal structure analysis

Single crystals of **1a**, **3a**, and **2b** suitable for X-ray diffraction were obtained by the slow diffusion of hexane into dichloromethane at room temperature. The C1–C2 and C3–C4 bond lengths in **BOISPY** are 1.469 and 1.479 Å, respectively, indicating a single-bond character. The single bond character suggests that the phenyl ring at the indolyl unit is rarely involved in the π -conjugation system. This is consistent with theoretical calculations and spectral properties. In contrast, the C2–N1 bond length in **BOINPY** is 1.410–1.420 Å, which is more conducive to the delocalization of electrons in the indole and pyridine units, the red-shifted absorption maximum can be attributed to this delocalization. The boron atom of **BOINPY** is coordinated in a tetrahedral geometry by two nitrogen atoms and two fluorine atoms or carbon atoms of the phenyl group (Fig. 2). The B–N (pyridyl or thiazolyl nitrogen) bond lengths are larger than the B–N bond lengths (indoline nitrogen) because of the asymmetric structure.^{14a,21} The core was nearly planar, and partially overlapping head-to-head or head-to-tail π - π stacking interactions were observed (Fig. S3, ESI†).

Photophysical properties

The photophysical properties of the prepared dyes were investigated in different solvents and films, and the results are summarized in Tables 1 and S2.† The absorbance maxima of **BOINPYs** (**1b–3b** and **4a–4c**) were observed in the wavelength ranges of 518–644 nm and 527–720 nm in dichloromethane and film, respectively (Fig. 3a and b). Usually, replacing F with an aromatic group at the boron of BODIPY did not affect the absorption wavelength; however, a large redshift (75–94 nm) of the absorption maximum was observed for **BOINPY**, because the electron-donating phenyl group participated in the frontier MO and decreased the band gap. The absorption bands on the film were broader, with a redshift of the absorbance maxima to 720 nm (for **2b**) owing to π - π stacking. The absorption maxima did not show any clear trend as a function of the solvent polarity (Fig. S4, ESI†). Notably, unlike BOISPY, these molecules have high molar extinction coefficients of absorption ($\epsilon_{\text{max}} = 1.69\text{--}7.22 \times 10^4 \text{ M}^{-1} \text{ cm}^{-1}$) and negligible fluorescence quantum yields (<1%) (Tables 1, S2 and Fig. S4, S5, ESI†), indicating highly efficient nonradiative processes in the excited states originating from the nonradiative CI pathway. The photostability was assessed, and the absorption did not decrease beyond 3% in any case after 30 min of irradiation (Fig. 3c and d). However, the reference dyes rhodamine 6G and MB were quickly decomposed. The yields of singlet oxygen generation were significantly low (<8%) (Fig. S6 and S7, ESI†). Therefore, the **BOINPY** system is sufficiently stable and suitable for PTT.

Photothermal studies in solution and *in vitro*

2b and **4a–4c** were selected for the investigation of photothermal performance. The temperature of **2b** in DMF increased from 25 to 45 °C within 15 min upon irradiation with a 650 nm laser of

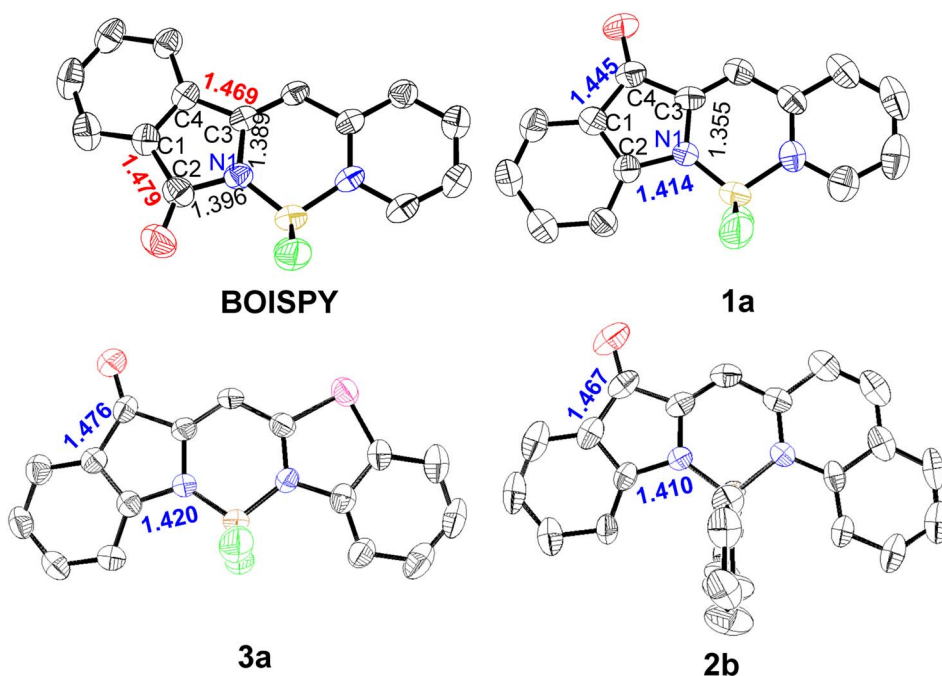


Fig. 2 ORTEP views of the molecular structures of **BOISPY**, **1a**, **3a**, and **2b** with thermal ellipsoids set at 50% probability.



Table 1 Photophysical and photosensitising properties of compounds **1a–4c**

Compounds	$\lambda_{\text{abs}}/\text{nm}$		$\lambda_{\text{em}}/\text{nm}$	Φ_{F}^a	Φ_{Δ}^b
	DCM	Film	2-MeTHF	2-MeTHF	
1a	518	527	591	0.006	n.d. ^c
2a	552	567	621	0.005	n.d.
3a	534	576	606	0.003	n.d.
1b	593	644	660	0.004	1.5%
2b	644	720	711	0.002	2.2%
3b	618	672	690	0.003	n.d.
4a	608	645	671	0.005	8%
4b	625	660	680	0.006	n.d.
4c	621	639	685	0.004	n.d.

^a Absolute fluorescence quantum yield (Φ_{F}) upon irradiation at the corresponding absorption maxima. ^b Singlet oxygen quantum yield (Φ_{Δ}) is determined using Rose Bengal (RB) for **1a–3a** ($\Phi_{\Delta}(\text{RB}) = 0.75$ in methanol)²² and MB for **1b–3b** and **4a–4c** ($\Phi_{\Delta}(\text{MB}) = 0.57$ in DCM).²³ ^c n.d. = not detected, DCM = dichloromethane.

intensity 0.8 W cm^{-2} (Fig. S8a and b, ESI†). No significant change in temperature ($<3^\circ\text{C}$) was detected in the control of DMF. The temperature increase is more prominent at higher laser powers (Fig. S8c, ESI†). The concentration and laser power dependence of **2b** indicated that the heat generation could be controlled as desired. Furthermore, the heating and cooling curves were

examined to determine the photothermal conversion efficiency (Fig. S8d, ESI†). Based on the corresponding thermal time constant, the photothermal conversion efficiency (η) of **2b** was determined to be 56.9% (Fig. S8e, ESI†). Notably, even after four on-and-off cycles with 650 nm laser irradiation, the maximum temperature of **2b** did not decrease significantly (Fig. S8f, ESI†), demonstrating the outstanding photothermal stability of **2b**. Thus, **2b** could efficiently convert light into heat and serve as a good contrast agent for PTT. The photothermal conversion efficiencies of **4a–4c** were calculated to be 55.3%, 50.1%, and 52.7%, respectively (Fig. S9, ESI†), indicating that structural modification based on this chromophore core is an intriguing strategy to design high-performance photothermal agents.

Encouraged by the good NIR absorption capacity and theoretical computation, **2b** was selected for the *in vitro* and *in vivo* photo-treatment investigation. To evaluate the therapeutic efficacy of the **2b**-based photothermal agent in living systems, we fabricated the nanomedicine *via* simple encapsulation with Pluronic F127 as an encapsulation matrix to improve the biocompatibility of **2b**. As shown in Fig. 4a, the spherical morphology of **2b**@F127 could be observed in the transmission electron microscopy (TEM) image while a hydrodynamic size of about 81.8 nm was tested by dynamic light scattering (DLS), which contributed to their accumulation at the tumour parts. Meanwhile, the UV-vis absorbance spectra also confirmed the

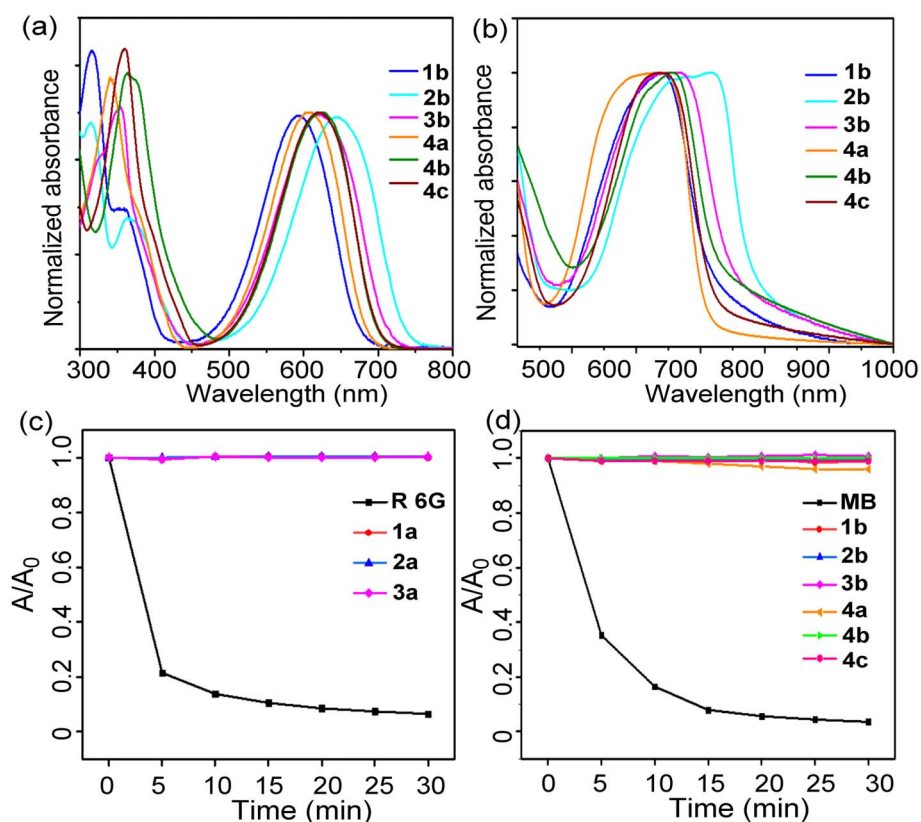


Fig. 3 Normalized absorption spectra of **1b–3b** and **4a–4c** in dichloromethane (a) and in drop-cast film on a quartz plate (b) at 293 K. (c) and (d) Photostability in dichloromethane upon irradiation with a laser beam (560 nm for **1a–3a**, rhodamine 6G as the reference compound; 635 nm for **1b–3b** and **4a–4c**, methylene blue as the reference compound) for 30 min (dye concentration = $5.0 \mu\text{M}$, 298 K).



successful encapsulation of **2b** in Pluronic F127. The absorption maximum of **2b**@F127 was slightly redshifted relative to that of **2b** in DMF due to aggregation (Fig. 4b). The absorption maximum at 650 nm is in good agreement with that of commercial lasers. **2b**@F127 has excellent water solubility and structural stability, with almost no change observed for hydrodynamic diameter while stored in the refrigerator at 4 °C for one week in the normal physiological environment (Fig. 4c). We then explored whether **2b**@F127 was an effective photothermal agent in aqueous media. The temperature changes at different concentrations of **2b**@F127 upon laser irradiation were recorded (Fig. 4d). The temperature reaches up to 35 °C at concentrations of 100 $\mu\text{mol L}^{-1}$ upon irradiation for 900 s at an intensity of 0.5 W cm^{-2} . As shown in Fig. 4e, the photothermal conversion efficiency (η) of **2b**@F127 was 44.2%, based on the photothermal effects and the time constant. This η value is higher than those of most photothermal agents²⁴ like Cu_9S_5 nanoparticles (*ca.* 25.7%) and indocyanine green (ICG) (*ca.* 12.1%). After irradiation for 5 min with a 650 nm laser (0.5 W cm^{-2}), the temperature of the **2b**@F127 solution increased from

23 to 40 °C and a small change was observed for the PBS-only sample (Fig. 4f). In addition, the biocompatibilities of **2b**@F127 were investigated by the hemocompatibility assays using a healthy mouse's red blood cells (RBCs). There was no observable hemolysis occurrence in either PBS or **2b**@F127 solution under the studied concentration range and time (Fig. 4g).

Having verified the photochemical and photophysical properties of **2b**@F127 in solution, we next investigated the photothermal potential at cellular levels with HeLa cancer cells. As displayed in Fig. 4h, the low dark cytotoxicity of **2b**@F127, even at a high concentration up to 100 μM , was found by co-incubation with HeLa cells using the standard Cell Counting Kit 8 (CCK-8). **2b**@F127 exerted significant concentration-dependent cytotoxicity towards cells, and the cell viability was inhibited down to 8% at a dose of 100 μM when exposed to a 650 nm laser (Fig. 4i). Then, intracellular generation of reactive oxygen species (ROS) by **2b**@F127 was investigated using 2',7'-dichlorofluorescein diacetate (DCFH-DA) as a probe, Fig. S10† shows that **2b**@F127 can generate intracellular ROS upon NIR light irradiation. We next investigated

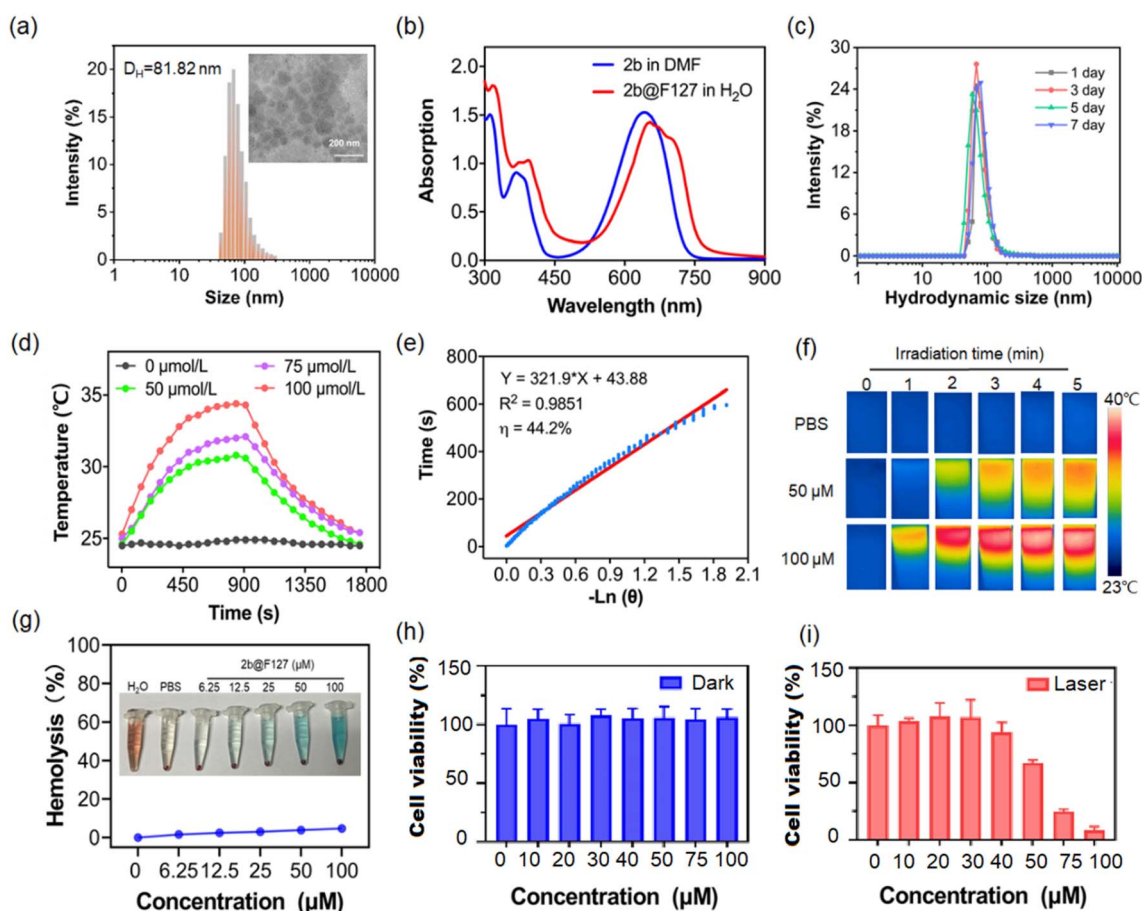


Fig. 4 (a) Hydrodynamic diameter distribution and TEM images (inset) obtained for **2b**@F127. (b) The absorption spectra of **2b** in DMF and **2b**@F127 in water. (c) Dynamic light scattering (DLS) curves of PBS of **2b**@F127 on different days of a week. (d) The photothermal effect of **2b**@F127 with different concentrations after irradiation by 650 nm laser (0.5 W cm^{-2}) for 30 min. (e) Cooling time of **2b**@F127 vs. negative log of temperatures and the linear fitting curve. (f) The photothermal photographs of **2b**@F127 ($\lambda_{\text{ex}} = 650 \text{ nm}$, 0.5 W cm^{-2}) using an FLIR E53 thermal imaging camera. (g) Hemolysis assay of **2b**@F127 against mice red blood cells (RBCs). (h) and (i) Cell viability of HeLa cells incubated with different concentrations of **2b**@F127 for 24 h without and with 650 nm (0.5 W cm^{-2}) laser irradiation.



the **2b**@F127-mediated therapeutic efficacy in cells. This was also intuitively demonstrated by live-dead cell staining using confocal laser scanning microscopy (CLSM), by co-staining with calcein AM (live, green fluorescence), and PI (dead, red fluorescence). As depicted in Fig. S10e,† the **2b**@F127 + laser group treated cells showed the highest cell-killing effect. Additionally, we determined the role of **2b**@F127 for phototherapy to induce DNA damage on clone formation (Fig. S10f†). A significantly decreased number of colonies was found in **2b**@F127, compared with the control

groups. These results confirmed that the photothermal effect of **2b**@F127 could effectively kill tumor cells.

In vivo animal experiments

Encouraged by the excellent photothermal properties of **2b**@F127 *in vitro*, photothermal therapy was performed *in vivo*. Tumour-bearing nude mice were randomly divided into two groups, named “PBS” and “**2b**@F127”. The HeLa-tumour-bearing mice

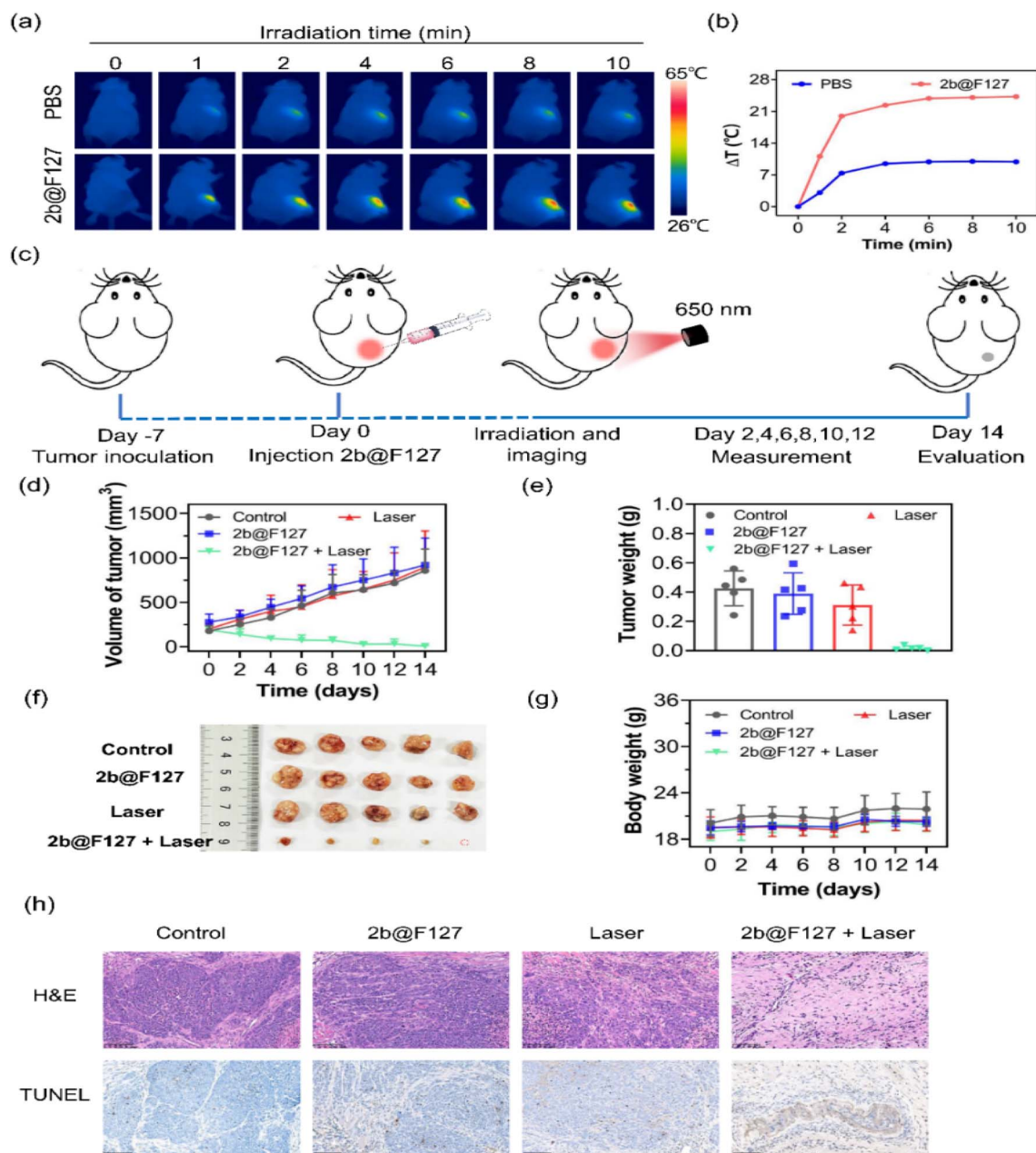


Fig. 5 (a) Thermal imaging of HeLa-tumour-bearing mice subjected to laser irradiation for 10 min after intra-tumour injection of PBS or **2b**@F127 ($200 \mu\text{M}$, $\lambda_{\text{ex}} = 650 \text{ nm}$, 0.5 W cm^{-2}). (b) Temperature variation in the tumour region within 10 min. (c) Schematic diagram of tumor-bearing mice model establishment and treatment operation. The mice in the treated groups were injected with **2b**@F127 and the tumor sites were irradiated with a 650 nm laser (0.5 W cm^{-2} , 10 min) after the injection. (d) Tumor volumes of the mice in the different groups during the observation period ($n = 5$). (e) Average weights of tumors collected from mice 14 days after initiation of various treatments. (f) Digital photos of excised tumors from the mice after 14 days under different treatment conditions as indicated. (g) Body weights of the mice in different groups during the observation period. (h) Tumor tissues of each group after photothermal therapy were stained by hematoxylin and eosin (H&E), and TUNEL (scale bar: $100 \mu\text{m}$).



were treated with intra-tumour injections of PBS or **2b**@F127 (200 μM), following which both the groups were exposed to a 650 nm laser for 0–10 min. The thermal images were continuously obtained with an IR thermal camera to monitor the temperature change at the tumour site upon laser irradiation. The thermal signals reached their maximum after 6 min. As shown in Fig. 5a and b, upon laser irradiation, the mice treated with **2b**@F127 showed an approximate increase of 26 $^{\circ}\text{C}$ within 10 min, which was reasonably higher than that observed for the mice treated with PBS only. Thus, **2b**@F127 underwent effective photothermal conversion *in vivo*.

Subsequently, in order to investigate the therapeutic efficacy of **2b**@F127 towards solid tumours, we further implemented an antitumor study on nude mice bearing HeLa tumours (Fig. 5c). These tumour-bearing mice were randomly divided into four groups (PBS, **2b**@F127, laser, and **2b**@F127 + laser). All mice were intratumor injected with **2b**@F127 or control samples (PBS), and then subjected to laser exposure (650 nm, 0.5 W cm^{-2} for 10 min). During the 14 days treatment period, the tumor volumes and body weights were measured every 2 days. As shown in Fig. 5d–f, it was found that the control, **2b**@F127, and laser groups exhibited negligible therapeutic effects on tumor growth. In the **2b**@F127 + laser group, the tumor growth was obviously inhibited and the size was smaller and even disappeared compared to the other groups, showing that **2b**@F127 exhibited exceptional anti-tumor efficacy under laser irradiation. Additionally, the body weight of mice in all four groups showed a slightly increasing trend throughout the 14 days tumor treatment period (Fig. 5g), demonstrating that **2b**@F127 had low biotoxicity and high biocompatibility. These results clearly demonstrated that high performance in the cure of solid tumors could be achieved by the **2b**@F127-enabled phototherapy under laser irradiation. To further investigate the PTT effect and biosecurity of **2b**@F127, hematoxylin & eosin (H&E) staining and a terminal deoxynucleotidyl transferase-mediated dUTP nick end labeling (TUNEL) assay of tumor sections were performed. H&E-staining of the tumor slices indicated that the **2b**@F127 + laser-treated group achieved the best treatment efficacy, while no obvious apoptotic/necrotic tissues were observed in the other groups. Moreover, the TUNEL assay results displayed a significant increase in the amount of apoptotic chromatin in the tumors treated with **2b**@F127 under laser irradiation. In addition, the *in vivo* systemic toxicity to main organs was also evaluated by monitoring H&E staining. **2b**@F127 showed no significant damage to normal tissues, including the heart, liver, spleen, lung, and kidney of the mice (Fig. S11, ESI†). Overall, these results validated that **2b**@F127 possesses a potential application for PTT.

Conclusions

In summary, we have developed a class of **BOINPY** derivatives with modular synthesis and high yields. They exhibited negligible emission, extremely low singlet oxygen production capability, superior photostability, and high photothermal conversion efficiencies. These results demonstrated that the **BOINPY** core provides a versatile construction kit for the design of PTA. As illustrated here for a series of **BOINPY** derivatives, the molecular platform enables structural modification with diversity and

meanwhile retains the photothermal properties. Moreover, we have shown that a high-efficiency photothermal agent can be rationally designed through a PIND process under NIR-laser irradiation. *In vitro* and *in vivo* investigations revealed that chromophore@F127 can serve as an efficient photothermal agent for tumour theranostics with minimized side effects for other tissues. Theoretically, PIND-guided photothermal molecules should have quantitative photothermal efficiency. For **BOINPY**, the energy of the CI state is higher than that of the $S_{0\text{min}}$ and $S_{1\text{min}}$ states, it needs to consume a certain amount of energy to cross the energy barrier. The design of photothermal molecules, in which the energy of the CI state is lower than those of the $S_{0\text{min}}$ and $S_{1\text{min}}$ states, is now ongoing. This work provides a novel photothermal molecular platform and a deeper understanding for exploring organic NIR-absorbing PTA for practical applications.

Ethical statement

All the animal experiments were performed in strict accordance with the National Institutes of Health Guide for the Care and Use of Laboratory Animals and were approved by the Institutional Animal Care and Use Committee of the Peking University First Hospital (Beijing, China).

Data availability

The ESI† includes all experimental details, including TD-DFT calculations, spectroscopic measurements, X-ray analysis, synthesis and characterization of all products reported in this study. NMR spectra of all products are included as well.

Author contributions

H. L., J. Z. and Z. G., supervised the work. L. G., X. S., S. W. and R. Z. conducted the experiments. H. L. and Z. N. performed the theoretical calculations. H. L., L. G. and J. Z. wrote the manuscript. All authors have been involved in checking the data, and have approved the final version of the manuscript.

Conflicts of interest

There are no conflicts to declare.

Acknowledgements

Financial support was provided by the National Natural Science Foundation of China (Grants No. 21871072, 21801057, 21571007, 21621061, 21778002, and 21861162008), the Chemistry and Chemical Engineering Guangdong Laboratory (1932002) and theoretical calculations were carried out at the Computational Centre for Molecular Design of Organosilicon Compounds, Hangzhou Normal University.

Notes and references

- 1 R. L. Siegel, K. D. Miller and A. Jemal, *Ca-Cancer J. Clin.*, 2020, **70**, 7–30.



- 2 K. Mortezaee, A. Narmani, M. Salehi, H. Bagheri, B. Farhood, H. Haghi-Aminjan and M. Najafi, *Life Sci.*, 2021, **269**, 119020.
- 3 (a) Y. Liu, P. Bhattarai, Z. Dai and X. Chen, *Chem. Soc. Rev.*, 2019, **48**, 2053–2108; (b) W. Fan, B. Yung, P. Huang and X. Chen, *Chem. Rev.*, 2017, **117**, 13566–13638; (c) L. Cheng, C. Wang, L. Feng, K. Yang and Z. Liu, *Chem. Rev.*, 2014, **114**, 10869–10939; (d) J. Huo, Q. Jia, H. Huang, J. Zhang, P. Li, X. Dong and W. Huang, *Chem. Soc. Rev.*, 2021, **50**, 8762–8789; (e) Q. Zheng, X. Liu, Y. Zheng, K. W. K. Yeung, Z. Cui, Y. Liang, Z. Li, S. Zhu, X. Wang and S. Wu, *Chem. Soc. Rev.*, 2021, **50**, 5086–5125.
- 4 N. Ni, X. Zhang, Y. Ma, J. Yuan, D. Wang, G. Ma, J. Dong and X. Sun, *Coord. Chem. Rev.*, 2022, **458**, 214415.
- 5 (a) G. Feng, G.-Q. Zhang and D. Ding, *Chem. Soc. Rev.*, 2020, **49**, 8179–8234; (b) H. S. Jung, P. Verwilt, A. Sharma, J. Shin, J. L. Sessler and J. S. Kim, *Chem. Soc. Rev.*, 2018, **47**, 2280–2297; (c) G. Xu, W. Guo, X. Gu, Z. Wang, R. Wang, T. Zhu, H. Tian and C. Zhao, *CCS Chem.*, 2020, **2**, 527–538.
- 6 (a) T. W. Liu, E. Huynh, T. D. MacDonald and G. Zheng, in *Cancer Theranostics*, Elsevier, 2014, pp. 229–254; (b) Z.-S. Yang, Y. Yao, A. C. Sedgwick, C. Li, Y. Xia, Y. Wang, L. Kang, H. Su, B.-W. Wang and S. Gao, *Chem. Sci.*, 2020, **11**, 8204–8213.
- 7 B.-D. Zheng, Q.-X. He, X. Li, J. Yoon and J.-D. Huang, *Coord. Chem. Rev.*, 2021, **426**, 213548.
- 8 (a) Y. Cai, W. Si, Q. Tang, P. Liang, C. Zhang, P. Chen, Q. Zhang, W. Huang and X. Dong, *Nano Res.*, 2017, **10**, 794–801; (b) X. Jiang, L. Wang, H. Tang, D. Cao and W. Chen, *Dyes Pigm.*, 2020, **181**, 108599.
- 9 K. Bilici, S. Cetin, E. Aydinoglu, H. Yagci Acar and S. Kolenen, *Front. Chem.*, 2021, DOI: [10.3389/fchem.2021.707876](https://doi.org/10.3389/fchem.2021.707876).
- 10 (a) M. Zhao, Q. Zeng, X. Li, D. Xing and T. Zhang, *Nano Res.*, 2022, **15**, 716–727; (b) C. Ma, T. Zhang and Z. Xie, *J. Mater. Chem. B*, 2021, **9**, 7318–7327; (c) D. Chen, Z. Zhong, Q. Ma, J. Shao, W. Huang and X. Dong, *ACS Appl. Mater. Interfaces*, 2020, **12**, 26914–26925.
- 11 C. Xu and K. Pu, *Chem. Soc. Rev.*, 2021, **50**, 1111–1137.
- 12 J. S. Ni, X. Zhang, G. Yang, T. Kang, X. Lin, M. Zha, Y. Li, L. Wang and K. Li, *Angew. Chem., Int. Ed.*, 2020, **132**, 11394–11398.
- 13 Y. Zhou, Y. Xiao, D. Li, M. Fu and X. Qian, *J. Org. Chem.*, 2008, **73**, 1571–1574.
- 14 (a) H. Liu, H. Lu, J. Xu, Z. Liu, Z. Li, J. Mack and Z. Shen, *Chem. Commun.*, 2014, **50**, 1074–1076; (b) H. Liu, H. Lu, Z. Zhou, S. Shimizu, Z. Li, N. Kobayashi and Z. Shen, *Chem. Commun.*, 2015, **51**, 1713–1716; (c) Y. Wu, H. Lu, S. Wang, Z. Li and Z. Shen, *J. Mater. Chem. C*, 2015, **3**, 12281–12289; (d) H. Liu, Y. Wu, Z. Li and H. Lu, *J. Porphyrins Phthalocyanines*, 2014, **18**, 679–685; (e) H. Zhang, Y. Wu, M. Fan, X. Xiao, J. Mack, G. Kubheka, T. Nyokong and H. Lu, *New J. Chem.*, 2017, **41**, 5802–5807; (f) H. Liu, H. Lu, F. Wu, Z. Li, N. Kobayashi and Z. Shen, *Org. Biomol. Chem.*, 2014, **12**, 8223–8229.
- 15 M. J. Frisch, G. W. Trucks, H. B. Schlegel, G. E. Scuseria, M. A. Robb, J. R. Cheeseman, G. Scalmani, V. Barone, G. A. Petersson, H. Nakatsuji, X. Li, M. Caricato, A. V. Marenich, J. Bloino, B. G. Janesko, R. Gomperts, B. Mennucci, H. P. Hratchian, J. V. Ortiz, A. F. Izmaylov, J. L. Sonnenberg, D. Williams-Young, F. Ding, F. Lipparini, F. Egidi, J. Goings, B. Peng, A. Petrone, T. Henderson, D. Ranasinghe, V. G. Zakrzewski, J. Gao, N. Rega, G. Zheng, W. Liang, M. Hada, M. Ehara, K. Toyota, R. Fukuda, J. Hasegawa, M. Ishida, T. Nakajima, Y. Honda, O. Kitao, H. Nakai, T. Vreven, K. Throssell, J. A. Montgomery Jr, J. E. Peralta, F. Ogliaro, M. J. Bearpark, J. J. Heyd, E. N. Brothers, K. N. Kudin, V. N. Staroverov, T. A. Keith, R. Kobayashi, J. Normand, K. Raghavachari, A. P. Rendell, J. C. Burant, S. S. Iyengar, J. Tomasi, M. Cossi, J. M. Millam, M. Klene, C. Adamo, R. Cammi, J. W. Ochterski, R. L. Martin, K. Morokuma, O. Farkas, J. B. Foresman and D. J. G. R. C. Fox, *Gaussian 16 (Revision A.03)*, Gaussian Inc., Wallingford, CT, 2016.
- 16 M. W. Schmidt, K. K. Baldridge, J. A. Boatz, S. T. Elbert, M. S. Gordon, J. H. Jensen, S. Koseki, N. Matsunaga, K. A. Nguyen and S. Su, *J. Comput. Chem.*, 1993, **14**, 1347–1363.
- 17 S. R. Billeter and A. Curioni, *J. Chem. Phys.*, 2005, **122**, 034105.
- 18 Z. Chen, C. S. Wannere, C. Corminboeuf, R. Puchta and P. v. R. Schleyer, *Chem. Rev.*, 2005, **105**, 3842–3888.
- 19 D. Geuenich, K. Hess, F. Köhler and R. Herges, *Chem. Rev.*, 2005, **105**, 3758–3772.
- 20 (a) J.-S. Ni, X. Zhang, G. Yang, T. Kang, X. Lin, M. Zha, Y. Li, L. Wang and K. Li, *Angew. Chem., Int. Ed.*, 2020, **59**, 11298–11302; (b) N. Inai, D. Yokogawa and T. Yanai, *J. Phys. Chem. A*, 2021, **125**, 559–569.
- 21 Y. P. Wu, S. S. Wang, Z. F. Li, Z. Shen and H. Lu, *J. Mater. Chem. C*, 2016, **4**, 4668–4674.
- 22 J. R. Wagner, H. Ali, R. Langlois, N. Brasseur and J. E. van Ller, *Photochem. Photobiol.*, 1987, **45**, 587–594.
- 23 F. Wilkinson, W. P. Helman and A. B. Ross, *J. Phys. Chem. Ref. Data*, 1993, **22**, 113–262.
- 24 (a) Y. Zou, M. Li, T. Xiong, X. Zhao, J. Du, J. Fan and X. Peng, *Small*, 2020, **16**, 1907677; (b) W. Zhang, W. Lin, C. Li, S. Liu, X. Hu and Z. Xie, *ACS Appl. Mater. Interfaces*, 2019, **11**, 32720–32728; (c) W. Sang, Z. Zhang, Y. Dai and X. Chen, *Chem. Soc. Rev.*, 2019, **48**, 3771–3810.

